

# Background Insensitive Polarization-Independent Ultra-Broadband Metamaterial Perfect Absorber in Mid-Infrared Regions

Hongyan Yang<sup>✉</sup>, Zhenkai Li, Ziyang Mei, Gongli Xiao<sup>✉</sup>, Hongchang Deng<sup>✉</sup>, and Libo Yuan<sup>✉</sup>

**Abstract**—The mid-infrared absorber is an important device for effective capture of high atmospheric infrared transparent window, and has been a research hotspot in military, medical, biological and other fields. In this paper, a kind of ultra-thin mid-infrared ultra-broadband absorber with background insensitive is realized by stacking four metal/dielectric films ( $\text{Si}/\text{Ag}/\text{Si}_3\text{N}_4/\text{SiO}_2$ ) on silver substrate and periodically arranged cross-anchor metal pattern in a method of finite-difference time domain. The results show that the absorption rate is more than 90% and the relative absorption bandwidth is 95.5% in the wavelength ranging from  $9.1 \mu\text{m}$  to  $24.1 \mu\text{m}$ . The average absorptivity is 92% in the range of background refractive index ( $n = 1\sim 1.8$ ). A proof of the device's insensibility to background refractive index. At a large incidence angle ( $\theta \leq 50^\circ$ ), the lowest absorption rate is up to 80%. The thickness of the optimized device is only  $1.7 \mu\text{m}$ . The research results have important application value in infrared remote sensing, pollution monitoring, disease diagnosis and other fields.

**Index Terms**—Background insensitive, ultra-broadband, metamaterial perfect absorber, mid-infrared.

## I. INTRODUCTION

METAMATERIAL are an artificial composite structure or composite material having extraordinary physical properties that natural materials do not have. This material has very broad application prospects in imaging, sensing, absorber and other fields [1] because of its ultra-thin size, high absorption efficiency, and highly controllable working range. Absorbers designed for traditional materials are larger and thicker, while metamaterial absorbers (MA) with a thickness of only a quarter wavelength or less are more suitable for micro-integrated optoelectronic systems [2]. In addition, due to the strong frequency select characteristics of metamaterial absorbers, the MA play an important role in the fields that traditional absorbers cannot

achieve. In 2008, Landy et al. [3] developed a near-perfect absorber and presented the notion of metamaterial perfect absorber (MPA) for the first time, the research of MPA has been sparked since then. According to the absorption bandwidth, the absorber can be split into broadband and narrowband absorption. Broadband absorption can be used in solar cells [4] and stealth vests [5]. Narrow band absorption can be used for sensing [6] and photoelectric detection [7]. However, the narrow working bandwidth due to the resonance characteristics of its sub-wavelength structure, which suggests the limitation of its future application. With the improvement of micro-nano processing technology in recent years, researchers have experimented various structures and materials to broaden the absorption band in the process of realizing perfect absorption. One is to enhance the resonance properties by designing metamaterial structures to achieve ultra-wideband, such as all dielectric array structure [8], stacking structure [9], coupling metal resonator structures of various sizes [10], conical structure [11] and three-dimensional spiral structure [12]. The other is to introduce the properties of emerging 2D materials, such as black phosphorus [13], graphene [14], molybdenum sulfide [15] and so on.

Most MPAs currently are designed to operate in visible [16], [17], infrared [18], [19], terahertz [20], [21], and microwave light [22], but with a less attention on absorbers in mid-infrared ( $2.5\sim 30 \mu\text{m}$ ). The mid-infrared light is located in the molecular fingerprint spectral region, covering multiple transmission windows of the earth atmosphere. The mid-infrared absorber is an important device for the effective capture of high-temperature targets for the atmospheric infrared transparent window, which is used widely in thermal imaging [23], infrared temperature measurement [24], and infrared camouflage [25]. In 2020, Yu Zhou et al. [26] designed a four-layer absorber with  $\text{Ti}/\text{Ge}/\text{Si}_3\text{N}_4/\text{Ti}$  structure, which had an average absorption of 94.5% in the range of  $8 \mu\text{m}$  to  $14 \mu\text{m}$ , and the absorber had an average absorption of more than 90% for plane waves in TE or TM modes with  $40^\circ$  incidence angle. In 2020, Song Yue et al. [27] proposed a multilayer absorber with sawtooth and pyramid shapes. Its working bandwidth extends from ultraviolet (UV) to long wave infrared (LWIR) through the effective hyperbolic metamaterial model and the excitation of various slow light modes, and it maintains an average absorption rate of more than 90% under the incident light of TM and EMT modes. In 2021, Shuaizhao Wang et al. [28] designed a dual-band wide-range tunable terahertz

Manuscript received 30 June 2022; revised 8 August 2022; accepted 21 August 2022. Date of publication 24 August 2022; date of current version 4 October 2022. This work was supported by the National Natural Science Foundation of China under Grant 62165004. (Corresponding author: Gongli Xiao.)

Hongyan Yang, Zhenkai Li, Ziyang Mei, Hongchang Deng, and Libo Yuan are with the School of Optoelectronic Engineering, Guilin University of Electronic Technology, Guilin 541004, China (e-mail: hyyang@guet.edu.cn; 19082203009@mails.guet.edu.cn; 19082203004@mails.guet.edu.cn; hcdeng@guet.edu.cn; lbyuan@guet.edu.cn).

Gongli Xiao is with the Guangxi Key Laboratory of Precision Navigation Technology and Application, Guilin University of Electronic Technology, Guilin 541004, China (e-mail: xiaogl.hy@guet.edu.cn).

Digital Object Identifier 10.1109/JPHOT.2022.3201267

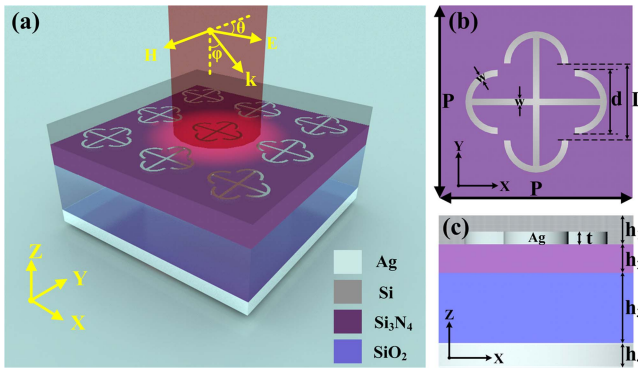


Fig. 1. (a) 3D schematic diagram of the proposed MPA structure. (b) Top view of the unit structure ( $x$ - $y$  plane). (c) Side view of the unit structure ( $x$ - $z$  plane).

absorber based on graphene and bulk Dirac semimetal (BDS), which absorption can almost achieve 100% at 3.97 Thz and 7.94 Thz. Moreover, that absorber can keep the similar absorption when the background refractive index  $n$  changes in the range of 1~1.4.

The above studies have their own characteristics in different structures and material designs. They all focus on bandwidth, absorbing efficiency and structure, and seldom focus on the performance and efficiency of absorbers in complex situation. The reason for a mid-infrared MPA that is insensitive to the background refractive index is to be proposed in this paper. That MPA has an average absorption of 95.5% in the range of  $9.1\ \mu\text{m}$  to  $24.2\ \mu\text{m}$  and has polarization-independent characteristics. The average absorption is up to 93% when the incident angle up to  $50^\circ$ . The lowest absorption is greater than 92% when the background refractive index  $n = 1\sim 1.8$ , the thickness dimension of the device was limited to  $1.7\ \mu\text{m}$ , which is less than an order of magnitude and smaller than the wavelength of incident light. This ultra-broadband and ultra-thin MPA can solve the application problems in complex military and medicine scenarios, and has substantial research significance for thermal imaging and night vision.

## II. MODEL DESIGN AND THEORETICAL ANALYSIS

The schematic diagram of the planned MPA is depicted in Fig. 1(a). The bottom metal substrate is silver, and the dielectric layers  $\text{SiO}_2$  and  $\text{Si}_3\text{N}_4$  are applied to the surface of metal substrate. The cross-anchor pattern is arranged on the layer  $\text{Si}_3\text{N}_4$  surface at regular intervals, and the material is silver. To avoid oxidation and corrosion of the cross-anchor, the top layer is covered with a Si dielectric layer. In this paper, the time domain finite difference software FDTD Solutions was used to simulate the structural dimensions and optical response of the device. To ensure correct periodic simulation, the simulation is set up with periodic boundary conditions in the  $x$  and  $y$  directions and perfectly matched layer conditions (PML) in the  $z$  direction to avoid unphysical scattering on the boundary, we set the background refractive index of the entire simulation space to 1.33 to simulate the ideal state of the aqueous solution environment. The light source is positioned directly above the device, and the simulated

TABLE I  
MPA OPTIMIZED STRUCTURAL PARAMETERS(UNIT/NM)

$h_1$	$h_2$	$h_3$	$h_4$	$t$	$w$	$d$	$L$	$P$
250	270	900	260	40	30	260	600	1600

plane wave is incident vertically (in the negative  $z$  direction) onto its surface, the polarization direction is  $x$  direction. The wavelength scan mode was employed to investigate the trend of absorption spectra as the incident wavelength changed. In Fig. 1(b), the outer diameter of the semicircular ring is  $d$ , the center distance of the semicircular ring is  $L$ , the line width is  $w$ , the optimized unit structure period is  $P$ , and  $h_1$ ,  $h_2$ ,  $h_3$  are the thicknesses of the layer Si, layer  $\text{Si}_3\text{N}_4$ , and layer  $\text{SiO}_2$ , respectively,  $h_4$  is the thickness of the metal substrate, and  $t$  is the cross-anchor height in Fig. 1(c). The optimized MPA structure parameters are shown in Table I.

Although we have only conducted a simulation study of the absorber, the feasibility of experimental manufacturing and the preparation process need to be taken into account. First, the silver substrate is deposited by thermal evaporation technology [29], then the underlying  $\text{SiO}_2$  can be deposited on the silver substrate by low pressure chemical vapor deposition (LPCVD) [30]. A plasma-enhanced chemical vapor deposition system (PECVD) sputtered 270 nm thickness  $\text{Si}_3\text{N}_4$  [31], followed by photoresist spin coating, lithography patterning, then development, deposition of cross-anchor by electron beam evaporation, the photoresist is dissolved by a lift-off process to form the metal pattern [32]. Finally, deposition of 250 nm Si is sputtered using the PECVD process [33], [34].

The two most essential indications of broadband absorbers are absorption rate and absorption bandwidth, and the relative absorption bandwidth (ABW) is defined as  $ABW = 2 \times (\lambda_{\max} - \lambda_{\min}) / (\lambda_{\max} + \lambda_{\min})$ , where  $\lambda_{\max}$  and  $\lambda_{\min}$  are the maximum and minimum wavelengths of the absorption band with an absorption rate greater than 90%. Absorption  $A(\omega) = 1 - R(\omega) - T(\omega) = 1 - |S_{11}|^2 - |S_{21}|^2$ , where  $R(\omega)$  is reflectance,  $T(\omega)$  is transmittance,  $S_{11}$  and  $S_{21}$  denote the scattering parameters relevant to reflection and transmission coefficients, separately, which has the following relationship with MPA [35]:

$$\begin{cases} S_{11} = \frac{i}{2} \left( \frac{1}{z} - z \right) \sin(nkd) \\ S_{21} = \frac{1}{\cos(nkd) - \frac{i}{2} \left( z + \frac{1}{z} \right) \sin(nkd)} \end{cases} \quad (1)$$

Where  $n$  is the refractive index and  $k$  is the free space wave vectors,  $d$  represents the thickness of the dielectric slab,  $z$  is the wave impedance [36] of the dielectric slab. In general, the equivalent impedance of MPA may be made equal to the free space impedance by modifying structural characteristics. According to the  $S$ -parameter retrieval methods [35], the value of the equivalent impedance can be determined by measuring the phase and amplitude of the electromagnetic waves transmitted and reflected from the device, as follow:

$$Z = \pm \sqrt{\frac{(1 + S_{11})^2 - S_{21}^2}{(1 - S_{11})^2 - S_{21}^2}} \quad (2)$$

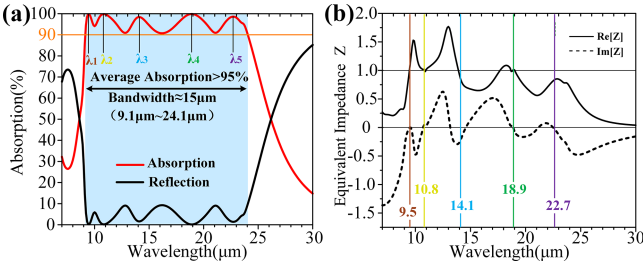


Fig. 2. (a) Absorption and reflection spectra of MPA. (b) The equivalent impedance curves of MPA. The black solid line is the real component of equivalent impedance, while the black dashed line is the imaginary component of equivalent impedance.

According to the impedance matching principle [37], when the equivalent impedance of device matches the free space impedance ( $\text{Re}[Z] = 1, \text{Im}[Z] = 0$ ), the reflection is completely suppressed, resulting in the absorption rate reaching its maximum. A sufficiently thick metal substrate will prevent incoming light from penetrating, the equation above may be simplified to:

$$Z = 1 + S_{11}/1 - S_{11} \quad (3)$$

The refractive index of silicon is set to 3.42. Optical constant of silicon dioxide is derived from the parametric mode of Palik, and the optical constants of silicon nitride in MIR were adopted from the experimental data of Kevin Luke et al. [38]. Relative permittivity of silver characterized through Drude mode:

$$\varepsilon(\omega) = \varepsilon_\infty - \frac{\omega_p^2}{\omega^2 + i\gamma\omega} \quad (4)$$

Here  $\omega$  is the angular frequency of incident light,  $\omega_p = 1.39 \times 10^{16} \text{ rad/s}$  is plasma frequency,  $\gamma = 2.7 \times 10^{13} \text{ rad/s}$  is metal loss factor, the metal dielectric constant at infinity frequency is  $\varepsilon_\infty$ , which is 3.4 at high frequency.

The red and black curves represent the absorption and reflectance of MPA in Fig. 2(a), respectively. The absorption bandwidth of MPA is 15 μm (9.1 μm~24.1 μm), and the relative absorption bandwidth is roughly 90.4%, with an average absorption of up to 95%. Fig. 2(b) shows a plot of the equivalent impedance versus wavelength for the MPA, demonstrating that the real and imaginary components of the equivalent impedance corresponding to the five peaks of  $\lambda_1$  (9.5 μm),  $\lambda_2$  (10.8 μm),  $\lambda_3$  (14.1 μm),  $\lambda_4$  (18.9 μm),  $\lambda_5$  (22.7 μm) are near to 1 and 0. The impedance matching is excellent and matches to the five absorption peaks shown in Fig. 2(a).

### III. RESULTS AND DISCUSSION

Fig. 3(a)–(c) show the structure without cross-anchor, dielectric layers  $\text{SiO}_2$  and  $\text{Si}_3\text{N}_4$  and our structure, separately. The absorption spectra of the above three structures are shown in Fig. 3(d). The absorption spectra without cross-anchored structure are shown by the red curves in Fig. 3(d), and the development of absorption peaks at 9.5 μm, 11.7 μm, and 22 μm is due to material absorption loss. In order to avoid the effect of absorption by lossy materials, we used a lossless medium with a refractive index of 2.5 in place of the dielectric layers  $\text{SiO}_2$  and  $\text{Si}_3\text{N}_4$ . In this situation, the absorption peaks at

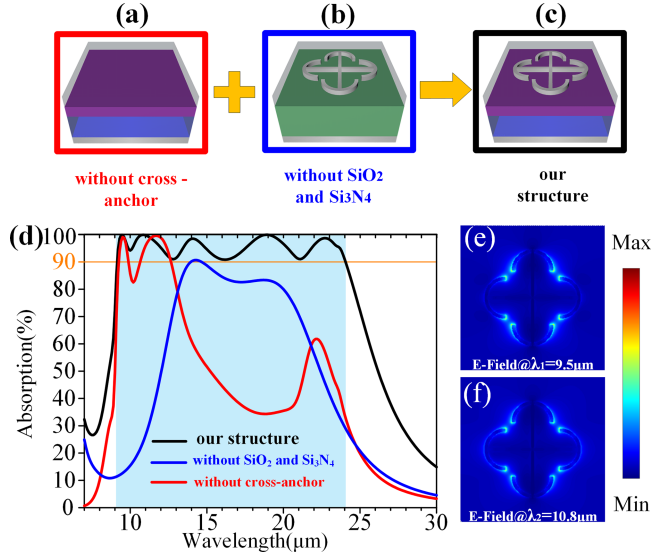


Fig. 3. (a) Absorption spectra of MPA without cross-anchor(red). (b) Absorption spectra of MPA without layers  $\text{SiO}_2$  and  $\text{Si}_3\text{N}_4$ . (c) The combined structure of both(black). (d) Absorption spectra under different materials and structures. (e-f) The electric field intensity distributions of the cross-anchor surface.

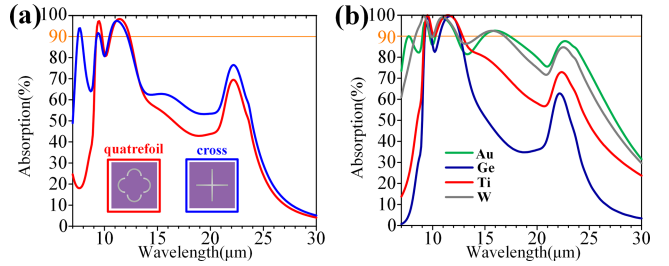


Fig. 4. (a) Comparison of absorption spectra of different metal structures. (b) Comparison of absorption spectra of different metal materials.

14.1 μm and 18.9 μm are mainly from plasmon resonance on the surface of cross-anchor. The black curve is the absorption spectrum of the combination of the red curve and the blue curve. The superposition of the material absorption loss in the red curve and the resonance absorption in the blue curve ultimately generate an ultra-broadband absorption. The electromagnetic field distribution at 9.5 μm and 10.8 μm is shown in Fig. 3(e), (f). As can be observed, the electromagnetic field strength of the cross-anchor surface is low, and its coupling capacity to the incident light field is minimal; thus, the absorption impact at this time is largely due to material absorption loss. In Fig. 4(a), we comparing the absorption spectra of cross-like, quatrefoil, and cross-anchor structures. The cross-like and quatrefoil structures show a nearly identical trend of change between the range of 9.1 μm to 13 μm. Fig. 4(b) shows the comparison of the absorption spectra when the cross-anchor materials are gold (yellow), germanium (blue), titanium (red), and tungsten (gray). And it can be concluded that the appearance of the two absorption peaks is not related to the metal structure and materials in combination with Fig. 3(a).

Fig. 5(a1) (a2) (a3) demonstrates a surface current vector distribution of the cross-anchor. It can be seen that the cross

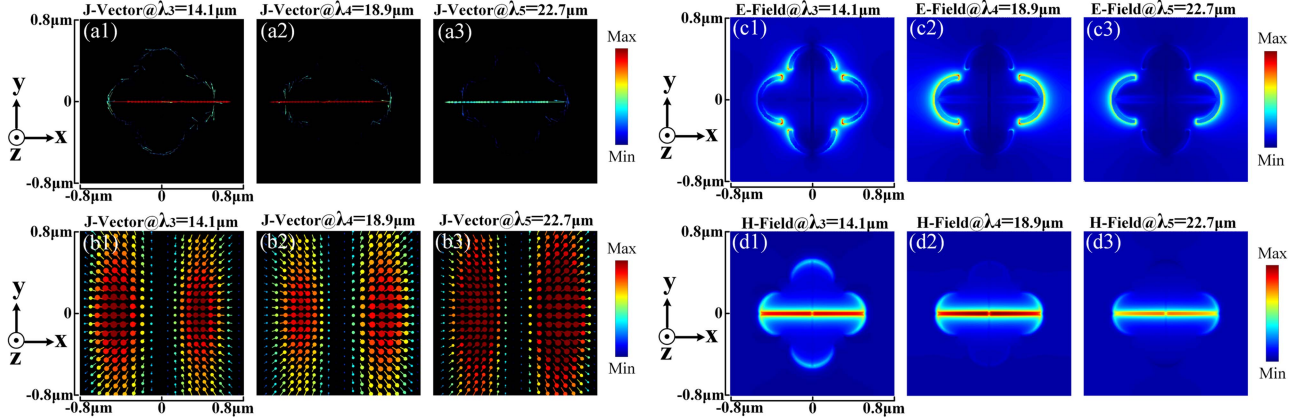


Fig. 5. The current vector distribution of the cross-anchor surface (a1-a3) and the bottom metal substrate surface (b1-b3) at three resonance peaks. The arrows representing the current direction. The electric field (c1-c3) and magnetic field (d1-d3) intensity distributions of the cross-anchor surface.

produces a current parallel to the direction of incident polarization, while the current flow direction of the metal substrate surface shown in Fig. 5(b1) (b2) (b3) is perpendicular to the direction of incident polarization, and the top and bottom metal structure surface currents are not parallel to each other, which means that no electrical resonance or magnetic resonance mode has been formed in the structure. To better understand the MPA absorption characteristics shown in the absorption spectrogram, we further investigated the electromagnetic field distribution on the cross-anchor surface at the locations of the three absorption peaks, and Fig. 5 shows the  $x$ - $y$  plane normalized electromagnetic field strength ( $|E|$ ) ( $|H|$ ). By observing Fig. 5(c1) (c2) (c3), we can see that the electric field is greatly enhanced at  $14.1 \mu\text{m}$ ,  $18.9 \mu\text{m}$  and  $22.7 \mu\text{m}$ . The electric field enhancement at  $14.1 \mu\text{m}$  is localized at both ends of the cross-anchored semicircle, which is the localized surface plasmon resonance (LSPR). The electric field enhancement at  $18.9 \mu\text{m}$  and  $22.7 \mu\text{m}$  occurs in the polarization direction of the cross-anchored semicircle, which is a typical electric dipole resonance. As shown in Fig. 5(d1) (d2) (d3), the charge within the cross-anchor will travel towards the ends under the operation of an external electromagnetic field to create a current, which creating a greater magnetic field. The incident light field energy is coupled into the electric and induced magnetic fields at both ends and eventually dissipated due to the ohmic thermal effect to achieve the effect of electromagnetic absorption.

Next, we explore the absorption characteristics of MPA by changing the structural dimensions of the cross-anchor, the cell period. The absorption spectra of different heights  $t$  are given in Fig. 6(a). The average absorption gradually increases when the height of the cross-anchor increases from  $20 \text{ nm}$  to  $40 \text{ nm}$ , and shows a decreasing trend when the height increases further. The absorption spectra for different line widths  $w$  are shown in Fig. 6(b), the absorption of MPA reaches a maximum at  $w = 30 \text{ nm}$  and then gradually decreases. Obviously, changing the structural parameters of the cross-anchor has a large impact on the intensity of the surface plasmon resonance, and optimization leads in the absorption rate reaching its maximum at  $w = 30 \text{ nm}$ ,  $t = 40 \text{ nm}$ . The effect of the half-circular circle center distance  $L$  on the absorption spectra is seen in Fig. 6(c). A huge amount

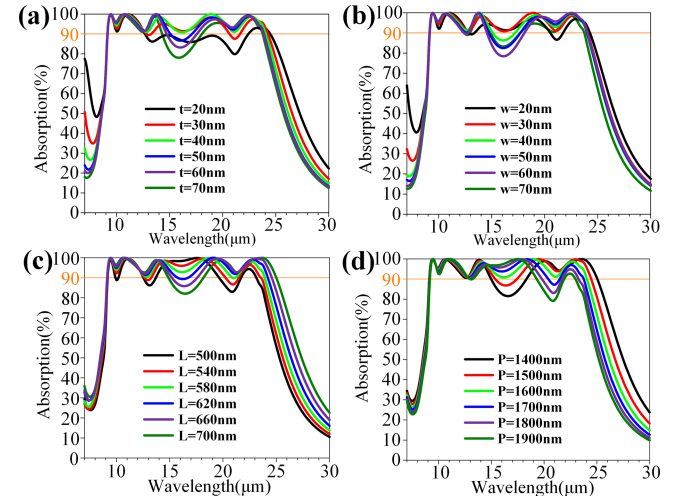


Fig. 6. Variation of absorption with respect to cross-anchor structural parameters and cell period. (a) Absorption spectra for different heights  $t$ . (b) Absorption spectra for different line widths  $w$ . (c) Absorption spectra for different semicircular ring centroid distances  $L$ . (d) Absorption spectra for different cell periods  $P$ .

of charge accumulates at the cross-anchor ends, generating an electric dipole resonance, and the increased dipole moment causes the  $18.9 \mu\text{m}$  and  $22.7 \mu\text{m}$  absorption peaks to redshift. Fig. 6(d) depicts the absorption spectra of several periods of the cell structure. The absorption peaks at  $18.9 \mu\text{m}$  and  $22.7 \mu\text{m}$  are blueshift when  $P$  increases from  $1400 \text{ nm}$  to  $1800 \text{ nm}$ . For parallel polarized light, the dipole oscillators between the units are mutually reinforcing when the period is much smaller than the incident light wavelength, which causing the resonance frequency to shift to high frequency [39].

Fig. 7(a) shows the complex refractive index data for diesel soot, water, and ice ( $\text{H}_2\text{O}$ ). The solid line represents the real part of the refractive index and the dashed line represents the imaginary part of the refractive index. Fig. 7(b) shows the absorption spectra of MPA with background environments of diesel soot, water, and ice ( $\text{H}_2\text{O}$ ), respectively. Fig. 7(c), (d) illustrates the equivalent impedance of the device in different background environments. It is found that the curve conforms to the absorption trend and the impedance

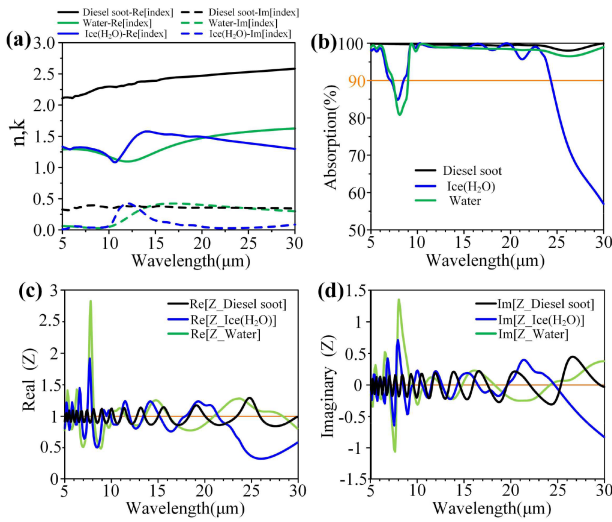


Fig. 7. (a) The complex refractive index data for diesel soot (black curve), water (green curve), and ice (blue curve). (b) The MPA absorption spectra in three background environments. (c) Equivalent impedance real part curves of devices in different environments. (d) Equivalent impedance imaginary part curves of devices in different environments.

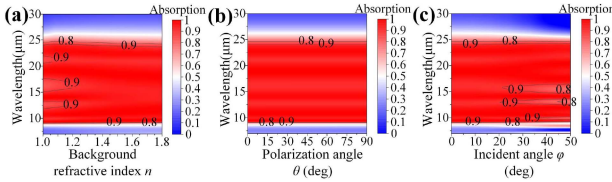


Fig. 8. (a) Absorption spectra for different background refractive indices  $n$ . (b) Absorption spectra for different polarization angles  $\theta$ . (c) Absorption spectra for different light incidence angles  $\varphi$ .

match is excellent, indicating that MPA still has outstanding absorption performance under the complex environments. The dispersion plot of the background refractive index  $n$  versus the absorption shown in Fig. 8(a). The refractive index range of 1 to 1.8 essentially covers the refractive index range of gases and liquids, and absorption performance improves as refractive index increases. From Fig. 8(b) that absorption is basically unchanged when  $\theta$  in the range of  $0^\circ$  to  $90^\circ$ , the polarization-independent property of this MPA is attributable to the rotational symmetry of the cross-anchor. As shown in Fig. 8(c), the absorption rate falls around  $13 \mu\text{m}$  and  $16 \mu\text{m}$  as  $\varphi$  increases from  $0^\circ$  to  $50^\circ$ , while the absorption maintains a high effect in the rest of the band.

#### IV. CONCLUSION

To summarize, the MPA suggested in this study, in contrast, is made up of four thin films and a metallic structure of periodically arranged cross-anchor with an average absorption of up to 95.5% performance in the range of  $9.1 \mu\text{m}$  to  $24.1 \mu\text{m}$  and polarization-independent. Our device overcomes the thickness limit of traditional  $1/4$  wavelength and has a thickness one order of magnitude smaller than the incident wavelength. The property of the lowest absorption is greater than 92% when the background refractive index  $n = 1\sim 1.8$  will lead to the

widespread use of this MPA for molecular detection, invisibility cloaks, infrared camouflage.

#### REFERENCES

- [1] N. I. Zheludev and Y. S. Kivshar, "From metamaterials to metadevices," *Nat. Mater.*, vol. 11, no. 11, pp. 917–924, Nov. 2012.
- [2] Y. S. Lin and Z. F. Xu, "Reconfigurable metamaterials for optoelectronic applications," *Int. J. Optomechatronics*, vol. 14, no. 1, pp. 78–93, Jan. 2020.
- [3] N. I. Landy, S. Sajuyigbe, J. J. Mock, D. R. Smith, and W. J. Padilla, "Perfect metamaterial absorber," *Phys. Rev. Lett.*, vol. 100, no. 20, 2008, Art. no. 207402.
- [4] N. J. Jeon et al., "Compositional engineering of perovskite materials for high-performance solar cells," *Nature*, vol. 517, no. 7535, pp. 476–480, Jan. 2015.
- [5] X. Ni, Z. J. Wong, M. Mrejen, Y. Wang, and X. Zhang, "An ultrathin invisibility skin cloak for visible light," *Science*, vol. 349, no. 6254, pp. 1310–1314, Sep. 2015.
- [6] N. Liu, M. Mesch, T. Weiss, M. Hentschel, and H. Giessen, "Infrared perfect absorber and its application as plasmonic sensor," *Nano Lett.*, vol. 10, no. 7, pp. 2342–2348, Jul. 2010.
- [7] J. Rosenberg, R. V. Shenoi, T. E. Vandervelde, S. Krishna, and O. Painter, "A multispectral and polarization-selective surface-plasmon resonant mid-infrared detector," *Appl. Phys. Lett.*, vol. 95, no. 16, 2009, Art. no. 161101.
- [8] K. Gorgulu, A. Gok, M. Yilmaz, K. Topalli, N. Biyikli, and A. K. Okyay, "All-silicon ultra-broadband infrared light absorbers," *Sci. Rep.*, vol. 6, Dec. 2016, Art. no. 38589.
- [9] D. Dong et al., "Designing a nearly perfect infrared absorber in monolayer black phosphorus," *Appl. Opt.*, vol. 58, no. 14, pp. 3862–3869, May 2019.
- [10] Z. Li, L. Stan, D. A. Czaplewski, X. Yang, and J. Gao, "Wavelength-selective mid-infrared metamaterial absorbers with multiple tungsten cross resonators," *Opt. Exp.*, vol. 26, no. 5, pp. 5616–5631, Mar. 2018.
- [11] Q. Liang, T. Wang, Z. Lu, Q. Sun, Y. Fu, and W. Yu, "Metamaterial-based two dimensional plasmonic subwavelength structures offer the broadest waveband light harvesting," *Adv. Opt. Mater.*, vol. 1, no. 1, pp. 43–49, 2013.
- [12] R. Mudachathi and T. Tanaka, "3D conical helix metamaterial-based isotropic broadband perfect light absorber," *Opt. Exp.*, vol. 27, no. 19, pp. 26369–26376 2019.
- [13] B. Tang, N. Yang, L. Huang, J. Su, and C. Jiang, "Tunable anisotropic perfect enhancement absorption in black phosphorus-based metasurfaces," *IEEE Photon. J.*, vol. 12, no. 3, Jun. 2020, Art no. 4500209.
- [14] S. Zhou et al., "Tunable chiroptical response of graphene achiral metamaterials in mid-infrared regime," *Opt. Exp.*, vol. 27, no. 11, pp. 15359–15367, May 2019.
- [15] Y. Zhong et al., "Tunable terahertz broadband absorber based on MoS<sub>2</sub> ring-cross array structure," *Opt. Mater.*, vol. 114, 2021, Art. no. 110996.
- [16] Q. Qian, T. Sun, Y. Yan, and C. Wang, "Large-area wide-incident-angle metasurface perfect absorber in total visible band based on coupled mie resonances," *Adv. Opt. Mater.*, vol. 5, no. 13, 2017, Art. no. 1700064.
- [17] P. T. Dang et al., "Efficient broadband truncated-pyramid-based metamaterial absorber in the visible and near-infrared regions," *Crystals*, vol. 10, no. 9, 2020, Art no. 784.
- [18] C. H. Fann, J. Zhang, M. ElKabbash, W. R. Donaldson, E. Michael Campbell, and C. Guo, "Broadband infrared plasmonic metamaterial absorber with multipronged absorption mechanisms," *Opt. Exp.*, vol. 27, no. 20, pp. 27917–27926, Sep. 2019.
- [19] Y. Zhou et al., "Small-sized long wavelength infrared absorber with perfect ultra-broadband absorptivity," *Opt. Exp.*, vol. 28, no. 2, pp. 1279–1290, Jan. 2020.
- [20] M. Kenney, J. Grant, Y. D. Shah, I. Escoria-Carranza, M. Humphreys, and D. R. S. Cumming, "Octave-spanning broadband absorption of terahertz light using metasurface fractal-cross absorbers," *ACS Photon.*, vol. 4, no. 10, pp. 2604–2612, 2017.
- [21] C. Sabah, B. Mulla, H. Altan, and L. Ozuyer, "Cross-like terahertz metamaterial absorber for sensing applications," *Pramana*, vol. 91, no. 2, pp. 1–7, 2018.
- [22] J. Zhang et al., "Ultra-broadband microwave metamaterial absorber with tetramethylurea inclusion," *Opt. Exp.*, vol. 27, no. 18, pp. 25595–25602, Sep. 2019.
- [23] D. Wen et al., "Helicity multiplexed broadband metasurface holograms," *Nat. Commun.*, vol. 6, Sep. 2015, Art. no. 8241.

- [24] F. A. Rhoads and J. Grandner, "Assessment of an aural infrared sensor for body temperature measurement in children," *Clin. Pediatr.*, vol. 29, no. 2, pp. 112–115, Feb. 1990.
- [25] N. Lee, J. S. Lim, I. Chang, H. M. Bae, J. Nam, and H. H. Cho, "Flexible assembled metamaterials for infrared and microwave camouflage," (in English), *Adv. Opt. Mater.*, vol. 10, no. 11, Jun. 2022.
- [26] Y. Zhou et al., "Broadband long wavelength infrared metamaterial absorbers," *Results Phys.*, vol. 19, 2020, Art. no. 103566.
- [27] S. Yue et al., "Ultra-broadband metamaterial absorber from ultraviolet to long-wave infrared based on CMOS-compatible materials," *Opt. Exp.*, vol. 28, no. 21, pp. 31844–31861, Oct. 2020.
- [28] S. Wang et al., "Wide-range tunable, dual-band, background refractive index insensitive terahertz absorber based on graphene and Dirac semimetal," *Opt. Eng.*, vol. 60, no. 2, 2021, Art. no. 027102.
- [29] D. M. Mattox, *Handbook of Physical Vapor Deposition (PVD) Processing*. Park Ridge, NJ, USA: William Andrew, 2010.
- [30] Y. Li, W. Liang, Y. Shi, and W. Zhou, "LPCVD-based SiO<sub>2</sub>/SiC multi-layers coating on graphite for improved anti-oxidation at wide-ranged temperatures," *Composites Part B-Eng.*, vol. 146, pp. 155–164, Aug. 2018.
- [31] C. Yang and J. Pham, "Characteristic study of silicon nitride films deposited by LPCVD and PECVD," *Silicon*, vol. 10, no. 6, pp. 2561–2567, Nov. 2018.
- [32] Z. J. Zhao et al., "Effects of polymer surface energy on morphology and properties of silver nanowire fabricated via nanoimprint and E-beam evaporation," *Appl. Surf. Sci.*, vol. 420, pp. 429–438, Oct. 2017.
- [33] A. G. Aberle, "Fabrication and characterisation of crystalline silicon thin-film materials for solar cells," *Thin Solid Films*, vol. 511, pp. 26–34, Jul. 2006.
- [34] J. K. Rath, M. Brinza, Y. Liu, A. Borreman, and R. E. I. Schropp, "Fabrication of thin film silicon solar cells on plastic substrate by very high frequency PECVD," *Sol. Energy Mater. Sol. Cells*, vol. 94, no. 9, pp. 1534–1541, Sep. 2010.
- [35] D. R. Smith, D. C. Vier, T. Koschny, and C. M. Soukoulis, "Electromagnetic parameter retrieval from inhomogeneous metamaterials," *Phys. Rev. E Stat. Nonlin Soft Mater. Phys.*, vol. 71, no. 3, Mar. 2005, Art. no. 036617.
- [36] D. Smith, R. Dalichaouch, N. Kroll, S. Schultz, S. McCall, and P. J. J. B. Platzman, "Photonic band structure and defects in one and two dimensions," *J. Opt. Soc. Amer. B*, vol. 10, no. 2, pp. 314–321, 1993.
- [37] P. Spinelli, M. Hebbink, R. de Waele, L. Black, F. Lenzmann, and A. Polman, "Optical impedance matching using coupled plasmonic nanoparticle arrays," *Nano Lett.*, vol. 11, no. 4, pp. 1760–1765, Apr. 2011.
- [38] K. Luke, Y. Okawachi, M. R. Lamont, A. L. Gaeta, and M. Lipson, "Broadband mid-infrared frequency comb generation in a Si<sub>3</sub>N<sub>4</sub> microresonator," *Opt. Lett.*, vol. 40, no. 21, pp. 4823–4826, Nov. 2015.
- [39] W. Rechberger, A. Hohenau, A. Leitner, J. R. Krenn, B. Lamprecht, and F. R. Ausenegg, "Optical properties of two interacting gold nanoparticles," *Opt. Commun.*, vol. 220, no. 1–3, pp. 137–141, 2003.
- [40] W. Guo, Y. Liu, and T. Han, "Ultra-broadband infrared metasurface absorber," *Opt. Exp.*, vol. 24, no. 18, pp. 20586–20592, Sep. 2016.
- [41] Y. Luo et al., "Ultra-broadband metamaterial absorber in long wavelength infrared band based on resonant cavity modes," *Opt. Commun.*, vol. 459, 2020, Art. no. 124948.
- [42] L. Li et al., "Ultra-broadband metamaterial absorber for infrared transparency window of the atmosphere," *Phys. Lett. A*, vol. 383, no. 36, 2019, Art. no. 126025.